Novel one-dimensional Bi2O3-Bi2WO6 p-n hierarchical heterojunction with enhanced photocatalytic activity

Journal:	*Journal of Materials Chemistry A*
Manuscript ID:	TA-ART-01-2014-000274.R1
Article Type:	Paper
Date Submitted by the Author:	14-Mar-2014
Complete List of Authors:	peng, yin; anhui normal university, College of Chemistry and Materials Science yan, mei; anhui normal university, College of Chemistry and Materials Science chen, qing; anhui normal university, College of Chemistry and Materials Science fan, cong; University of Science and Technology of China, Division of Nanomaterials and Chemistry zhou, hai; anhui normal university, College of Chemistry and Materials Science Xu, An-Wu; Hefei National Laboratory for Physical Sciences at Microscale, University of Science and Technology of China, Division of Nanomaterials and Chemistry

Novel one-dimensional Bi_2O_3-Bi_2WO_6 p-n hierarchical heterojunction with enhanced photocatalytic activity

Yin Peng[a], Mei Yan[a], Qing-Guo Chen[a], Cong-Min Fan[b], Hai-Yan Zhou[a] and An-Wu Xu*[b]

***Receipt/Acceptance Data* [DO NOT ALTER/DELETE THIS TEXT]**
***Publication data* [DO NOT ALTER/DELETE THIS TEXT]**
DOI: 10.1039/b000000x [DO NOT ALTER/DELETE THIS TEXT]

A novel one-dimensional (1D) Bi_2O_3 nanorods-Bi_2WO_6 nanosheets p-n junction photocatalyst was prepared by three steps synthetic route. The obtained products were characterized by X-ray diffraction (XRD), scanning electron microscopy (SEM), transmission electron mic-roscopy (TEM), high-resolution transmission electron microscopy (HRTEM), X-ray photoelectron spectroscopy (XPS), N_2-sorption/desorption and Brunauer-Emmett-Teller surface area (BET). Bi_2O_3 rods with the diameter of about 200 nm were obtained by calcining $Bi(OHC_2O_4)\bullet 2H_2O$ precursor. Bi_2WO_6 nanosheets vertically grow onto the Bi_2O_3 rods along the long axial direction. The photocatalytic activity to degrade Rhodamine B (RhB) and phenol under solar/visible light by p-n junction Bi_2O_3-Bi_2WO_6 nanorods was investigated. The result demonstrates that the novel Bi_2O_3-Bi_2WO_6 p-n heterostructures display higher photocatalytic activity than single Bi_2O_3 nanorods or Bi_2WO_6 flowers. The enhancement of the photocatalytic activity of the Bi_2O_3-Bi_2WO_6 p-n junction structures can be ascribed to the strong visible light absorption and the effective separation of photogenerated electrons and holes by the internal electrostatic field in the junction region. More importantly, 1D p-n heterostructures made of ordered nanosheets is beneficial for transport of photogenerated carriers, and increasing the rate of photocatalytic reaction. This work would offer a new insight into the design and fabrication of advanced materials with heterojunction structures for photocatalytic applications and optoelectronic devices.

Introduction

With the environmental pollution increase, green chemistry has become a necessary requirement for the sustainable development of human society. Among the various green chemical techniques, semiconductor photocatalysis has been considered an cost-effective, sustainable and the most promising green chemical technologie because it represents an easy way to complete degradation of organic pollutions by utilizing the solar energy.[1−3] However, some traditional photocatalysts (such as TiO_2, ZnO, SnO_2) can absorb only ultraviolet light due to their wide band gap and have moderate photocatalytic activity due to the high recombination rate of photogenerated carriers.[4−6] So, the development of photocatalysts performance under visible light constitutes the key point. A significant number of new photocatalysts do perform adequately under visible light but typically display poor performance with respect to TiO_2 commercial references (e.g., Degussa P25) under sunlight because the enhanced visible light absorption and fast recombination of charge recombination occurs simultaneously.[7] For that reason, instead of using a single semiconductor, combining two or more semiconductors with appropriate band positions to improve the photocatalytic performance is an established idea because it can lead to an enhanced charge separation and interfacial charge-transfer efficiency.[8-10] Especially, it is noted that the fabrication of a p-n junction photocatalyst is believed to be the very effective because of the existence of an internal electric field.[11,12]

As one of the simplest Aurivillius oxides with layered structure, Bi_2WO_6 is special for its good photocatalytic performance under visible light irradiation.[13−15] Bare Bi_2WO_6 presents photoabsorption properties from UV light to visible light with wavelength of shorter than ca. 450 nm,[16,17] which overlaps a small part of the solar spectrum. Moreover, the rapid recombination of photoinduced electron-hole pairs seriously limits the energy-conversion efficiency. To broaden the range of visible-light photoresponse and promote the separation of photogenerated carriers of Bi_2WO_6, we intend to design a composite photocatalyst by coupling Bi_2WO_6 with a narrow bandgap semiconductor Bi_2O_3 with matched band potentials. The well-established heterojunction structure could be employed to restrict the recombination of the charge carriers and enhance the quantum yield.[18] The electrons excited by visible light can be transferred to Bi_2WO_6 from the narrow bandgap semiconductor, which favors the charge separation and also improves the visible-light photocatalytic activity of the heterostructure dramatically. Bi_2O_3 is a p-type semiconductor with a band gap of 2.8 eV and has proved to be a photocatalyst for water splitting and pollutant decomposition under visible-light irradiation. However, the photocatalytic activity of pure Bi_2O_3 is also low because of the high recombination probability of photogenerated electrons and holes.[19−21] It is expected that the formation of p-n junction structure between n-type Bi_2WO_6 and p-type Bi_2O_3 will greatly enhance the photoctalytic efficiency. Recently, Bi_2O_3-Bi_2WO_6 p-n junction structures with microspheres,[22] hollow microspheres,[23,24] and flowers,[25,26] have been synthesized and exhibit better photocatalytic activies than pure Bi_2O_3 or Bi_2WO_6 samples. However, Bi_2O_3-Bi_2WO_6 p-n heterojunction with highly ordered Bi_2WO_6 nanosheets grown on one-dimensional (1D) Bi_2O_3 nanorods have not been reported. Compare with above mentioned heterostructures, 1D p-n heterojunction photocatalysts have aroused great concern because of their high surface areas,

---

[a]The Key Laboratory of Functional Molecular Solids, Ministry of Education, College of Chemistry and Materials Science, Anhui Normal University, Wuhu 241000, China
[b]Division of Nanomaterials and Chemistry, Hefei National Laboratory for Physical Sciences at Microscale, Department of Chemistry, University of Science and Technology of China, Hefei 230026, P. R China.
Fax: (+86) 551-6360 2346; E-mail: anwuxu@ustc.edu.cn.

† Electronic Supplementary Information (ESI) available: [details of any supplementary information available should be included here]. See http://dx.doi.org/10.1039/b000000x/

remarkable and directional transport characteristics of electrons and holes, and thus their enhanced photocatalytic activities.[27] Here, we report for the first time the synthesis of a novel Bi_2O_3 nanords-Bi_2WO_6 ordered nanosheets p-n junction via a simple method. This 1D heterostructure displays superior photocatalytic activity for degradation of the phenol and RhB under solar/visible light irradiation.

Experimental Section

Photocatalyst preparation

All the reagents used in our experiment were analytical grade and used as received without further purification.

$Bi(OHC_2O_4){\bullet}2H_2O$ nanorods were first synthesized via a hydrothermal method. $Bi(NO_3)_3{\bullet}5H_2O$ (2.911 g) and $Na_2C_2O_4$ (1.206 g) were dissolved separately in 20 mL distilled water. Then the $Na_2C_2O_4$ solution was added into the $Bi(NO_3)_3$ suspension solution with vigorous magnetic stirring. The mixed suspension solution was poured into a stainless steel autoclave with a Teflon liner and heated at 120 ºC for 40 h. The obtained solid sample was washed with deionized water and anhydrous ethanol, and then dried at 60 ºC for 6 h.

Then, Bi_2WO_6-$Bi(OHC_2O_4){\bullet}2H_2O$ samples were synthesized via a solvothermal process. 0.341 g of $Bi(OHC_2O_4){\bullet}2H_2O$ nanorods were added into the 15 ml of $Bi(NO_3)_3{\bullet}5H_2O$ ethylene glycol (EG) solution under magnetic stirring, and then 15 mL of $Na_2WO_4{\bullet}2H_2O$ aqueous solution was added drop-wise and stirred for another 30 min. The mixture was sealed into a Teflon-lined stainless steel autoclave and treated at 160 ºC for 20 h. After being cooled down to room temperature naturally, the products were collected and washed several times with deionized water and absolute ethanol, and dried at 60 ºC for 4 h. Bi_2WO_6 flowers were obtained in the absence of $Bi(OHC_2O_4){\bullet}2H_2O$ nanorods in above reactive system.

Finally, the Bi_2O_3-Bi_2WO_6 heterojunctions were obtained by calcining Bi_2WO_6-$Bi(OHC_2O_4){\bullet}2H_2O$ composites at 400 ºC for 2 h in air. The as-obtained samples with the molar ratio of $Bi(OHC_2O_4){\bullet}2H_2O$:$Bi_2WO_6$ 2:1.5, 2:3, 2:10, 2:2 and 2:4, were labelled WBP1, WBP2, WBP3, WBP4 and WBP5 respectively. And the corresponding calcined products Bi_2O_3-Bi_2WO_6 were labelled WB1, WB2, WB3, WB4 and WB5, respectively. Bi_2O_3 rods were obtained by calcinations of $Bi(OHC_2O_4){\bullet}2H_2O$ precursors at 400 ºC for 2 h in air.

Photocatalytic activity measurements

Photocatalytic activity of the prepared Bi_2O_3-Bi_2WO_6 samples was tested by decomposing phenol and RhB under solar/visible light irradiation. The light source was a 300 W Xe lamp (PLS-SXE300/300UV, Trusttech Co., Ltd. Beijing). In a typical experiment, the photocatalyst (100 mg) was added into 100 mL of phenol (or RhB) (10 mg/L) to produce a suspension for the degradation reaction at room temperature under air. Before the solar/visible light irradiation, the suspension was stirred in the dark for 30 min to ensure an adsorption/desorption equilibrium of phenol (or RhB) on the surface of the photocatalyst. Then, the suspension was illuminated by the Xe lamp combined with a UV cutoff filter ($\lambda \geq 400$ nm) under stirring. At given time intervals, above 4 mL suspension was withdrawn, and centrifuged to remove the precipitate. The degradation reaction process was monitored by measuring the concentration of phenol (or RhB) as a function of irradiation time in the solution with UV-Vis absorption spectra. Additionally, the recycling experiments were performed for six recycles to test the durability. After each cycle, the photocatalyst was centrifugation and used directly for the next test.

Photocatalytic water splitting

In a typical photocatalytic experiment, the prepared Bi_2O_3-Bi_2WO_6 sample (50 mg) was dispersed in an aqueous solution (100 mL) of $Fe_2(SO_4)_3$ (2.1 mM·L^{-1}). The suspension was sealed in a quartz flask and purged with argon for 1 h to drive away the residual air. The photocatalytic oxygen production was initiated by irradiating the suspension with a 300 W Xenon lamp (MAX-302, Asahi Spectra, USA) coupled with a UV cut-off filter ($\lambda >$ 420 nm). The gas product was analyzed periodically through a gas chromatograph (Agilent 7890A) with a thermal conductivity detector (TCD).

Characterization

Field emission scanning electron microscopy (FE-SEM) images were recorded on a Hitachi S-4800 microscope. Transmission electron microscopic (TEM) images, high-resolution transmission electron microscopic (HRTEM) images and the selected area electron diffraction (SAED) patterns were performed on a JEOL-2010 microscope with an accelerating voltage of 200 kV, and energy-dispersive X-ray spectroscopy (EDS) analysis was performed. X-Ray powder diffraction (XRD) was carried out on a Rigaku (Japan) D/max -γA X-ray diffractometer with Cu-Kα radiation (λ = 0.154178 nm). UV-vis diffuse-reflectance spectrum was recorded with a UV-2450 spectrophotometer in the wavelength range of 200-800 nm at room temperature. $BaSO_4$ was used as the reflectance standard material. The X-Ray photoelectron spectroscopy (XPS) was performed on a Perkin-Elmer RBD upgraded PHI-5000C ESCA system. Nitrogen adsorption/desorption measurements were performed at 77 K using a Micromeritics Tristar II 3020 M analyzer after the samples were degassed at 180 ºC for 6 h. The Brunauer-Emmett-Teller (BET) surface area was estimated by using adsorption data in a relative pressure range from 0.05 to 0.3.

Results and discussion

In this study, $Bi(OHC_2O_4){\bullet}2H_2O$ rods were first synthesized, then Bi_2WO_6-$Bi(OHC_2O_4){\bullet}2H_2O$ nanosheet-rod heterostructures were obtained by hydrothermal treatment using $Bi(OHC_2O_4){\bullet}2H_2O$ rods as support. Finally, Bi_2O_3-Bi_2WO_6 p-n junction nanostructures wit nanosheets standing on rods were prepared by calcinations of Bi_2WO_6-$Bi(OHC_2O_4){\bullet}2H_2O$. The $Bi(OHC_2O_4){\bullet}2H_2O$-$Bi_2WO_6$ heterostructures with different $Bi(OHC_2O_4){\bullet}2H_2O/Bi_2WO_6$ molar ratio of 2:1.5, 2:3 and 2:10, were labelled as WBP1, WBP2 and WBP3, respectively. And the corresponding calcined products Bi_2O_3-Bi_2WO_6 was denoted as WB1, WB2 and WB3, respectively (see experimental section).

The X-ray powder diffraction (XRD) patterns of the obtained products are shown in Fig. S1. All of the diffraction peaks in the Fig. S1a could be indexed to bismuth oxalate ($Bi(OHC_2O_4){\bullet}2H_2O$) precursor reported by Monnereau et al.[28] With the loaded-Bi_2WO_6 content increasing, the new diffraction peaks appear and their intensities increase gradually (Fig. S1 b-d) and these new peaks can be indexed to orthorhombic Bi_2WO_6 (Fig. S1e). These results show that the heterostructure between $Bi(OHC_2O_4){\bullet}2H_2O$ and Bi_2WO_6 is formed.

Fig. 1 shows the XRD patterns of obtained Bi_2O_3 rods, Bi_2O_3-Bi_2WO_6 p-n heterojunctions and Bi_2WO_6. All of the diffraction peaks shown in Fig. 1b and f can be well-indexed to the monoclinic structure of Bi_2O_3 (JCPDS No. 76-1730) and orthorhombic Bi_2WO_6 (JCPDS No. 39-0256), respectively. The sharp diffraction peaks of both Bi_2O_3 and Bi_2WO_6 indicate their good crystallinity. No traces of other phases are detected, confirming the high purity of the samples. Fig. 1c–e obviously show two sets of XRD peaks of monoclinic Bi_2O_3 and orthorhombic Bi_2WO_6, indicating that the as-synthesized products are composite materials. Moreover, it is noted that the diffraction peaks of Bi_2O_3 are weakened with increasing Bi_2WO_6/Bi_2O_3 molar ratio (see red labels in Fig. 1b-e), while the peak intensities of Bi_2WO_6 increase gradually.

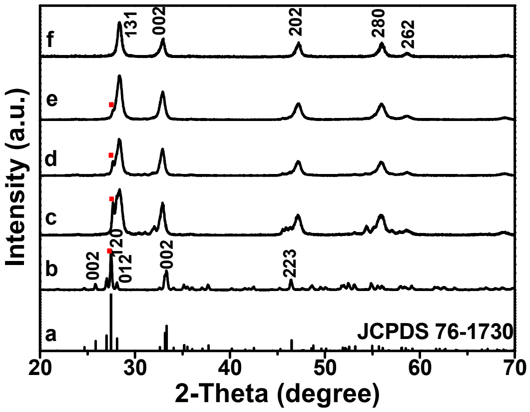

Fig. 1 The XRD patterns of (a) Standard Card of Bi_2O_3, (b) Bi_2O_3, (c) WB1, (d) WB2, (e) WB3 and (f) Bi_2WO_6.

Fig. 2 displayed the SEM images of these Bi_2O_3-Bi_2WO_6 heterojunctions and their precursors. $Bi(OHC_2O_4)•2H_2O$ is 1D rods with a mean diameter of 450 ± 50 nm and length of 5±1 μm. Each rod has smooth surface (Fig. 2a). After calcinations at 400 ºC for 2 h, $Bi(OHC_2O_4)•2H_2O$ transformed to Bi_2O_3 rods with rough surface and porosity due to gas removal (Fig. 2b). The obtained Bi_2WO_6-$Bi(OHC_2O_4)•2H_2O$ precursors are also 1D rod-like structures, and the thin Bi_2WO_6 nanosheets grow vertically onto the surface of $Bi(OHC_2O_4)•2H_2O$ nanorod (Fig. 2c). Meanwhile, the more the loaded-Bi_2WO_6 content is used, the more Bi_2WO_6 nanosheets orderly grow onto the $Bi(OHC_2O_4)•2H_2O$ rods along the long axial direction (Fig. 2e, g), and the gap between Bi_2WO_6 nanosheets becomes narrower and narrower, finally each $Bi(OHC_2O_4)•2H_2O$ rod is completely covered by Bi_2WO_6 nanosheets. During the formation of $Bi(OHC_2O_4)•2H_2O$-Bi_2WO_6 composite, the preferred outward diffusion of Bi ions from $Bi(OHC_2O_4)•2H_2O$ precursor to Bi_2WO_6 leads to a net material flux across the composite interface. Therefore, some hollow structures (see red arrows in Fig. 2e, g) are formed based on the Kirkendall effect.[29] From Fig. 2d, f, h, it can be clearly seen that the morphologies of the obtained Bi_2WO_6-Bi_2O_3 heterostructures were kept unchanged after calcining Bi_2WO_6-$Bi(OHC_2O_4)•2H_2O$ precursors at 400 ºC for 2 h.

To further obtain information about the structure of the sample, the WB2 p-n heterojunction was characterized by transmission electron microscopy (TEM). As shown in Fig. 3a, it can clearly seen the Bi_2WO_6 nanosheets vertically grow onto the surface of the Bi_2O_3 nanorods, which is consistent with the result of the SEM measurements. Fig. 3b shows the high-resolution transmission electron microscopic (HRTEM) image taken from the tip of the Bi_2WO_6 nanosheet (red square highlighted in Fig. 3a). It is found that two sets of lattice fringes with interplanar spacing of 0.82 nm and 0.27 nm, well correspond to (020) and (002) planes of orthorhombic Bi_2WO_6. The selected area electron diffraction (SAED) pattern (inset in Fig. 3b) taken from the nanoparticles can be indexed as a Bi_2WO_6 single crystal recorded along the [100] zone axis. The energy dispersive spectroscopy (EDS) analysis further confirms that nanosheets only contain O, Bi and W elements, and the atomic ratio of Bi/W is calculated to be about 1.85:1, close to 2:1 in Bi_2WO_6 (Fig. S2).

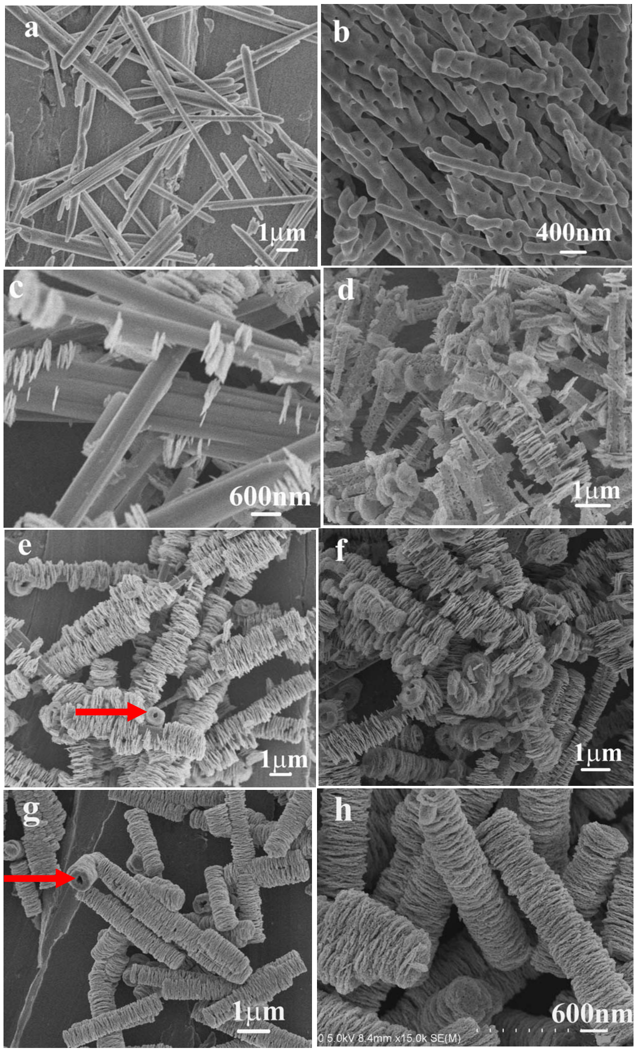

Fig. 2 The FE-SEM images of the Bi_2O_3-$Bi_2WO_6$and their precursors (a) $Bi(OHC_2O_4)•2H_2O$, (b) pure Bi_2O_3, (c) WBP1, (d) WB1, (e) WBP2, (f) WB2, (g) WBP3 and (h) WB3.

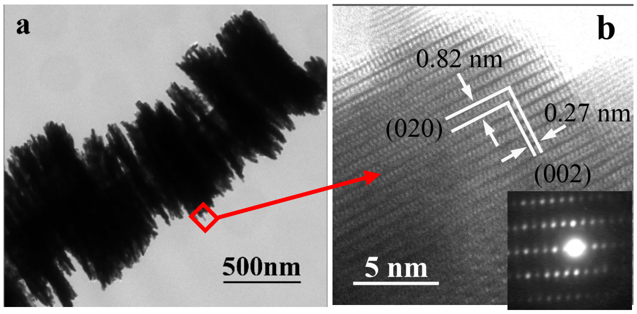

Fig. 3 (a) The TEM and (b) HRTEM images of the WB2 heterojunction.

Quantitative X-ray photoelectron spectroscopy (XPS) analysis was carried on the obtained WB2 heterostructures. The typical full survey and high-resolution spectra for Bi 4f, W 4f, and O 1s region were showed in Fig. 4. It can be seen that only O, Bi and W elements exist in the sample (Fig. 4a, (i)). High resolution XPS spectrum of W 4f region shows a binding energy at 35.5 eV for W $4f_{7/2}$ and at 37.6 eV for W $4f_{5/2}$, suggesting that W exists in the chemical state of W^{6+} (Fig. 5b, (i)).[22,30] The binding energy for Bi $4f_{5/2}$ and Bi $4f_{7/2}$ are 164.5 and 159.2 eV (Fig. 5c, (i)) respectively, which prove all the Bi species in the WB2 sample are in the form of Bi^{3+}. However, it is worth noting that these binding energy values are not exactly the same as those obtained from pure Bi_2O_3 or Bi_2WO_6,[30,31] which reveal that interfacial structure is formed and the local environment and electron density of the elements is changed in some degree. The XPS spectrum for O1s can be deconvoluted to three peaks at 529.6, 530.5 and 531.9 eV, which can be assigned to Bi-O and W-O in Bi_2WO_6 (Fig. 4d (i)) and Bi-O in Bi_2O_3, respectively.[23,25,31,32] On the other hand, according to the XPS result of sample WB2, the concentration of the surface Bi^{3+} is 20.66 atom%, whereas that of W^{6+} is 5.82 atom%. The atomic ratio of Bi and W is about 3.55, which is larger than the stoichiometric ratio in Bi_2WO_6. This result reveals the co-existence of Bi_2O_3 and Bi_2WO_6 species in the WB2 sample, in good accordance with the XRD, TEM and SEM results.

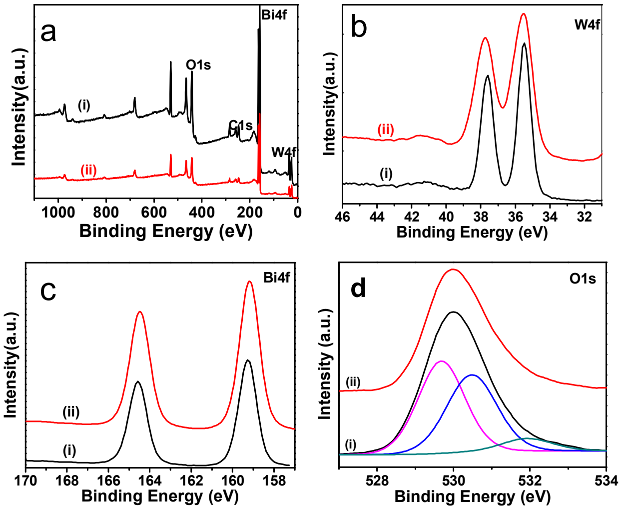

Fig. 4 (a) Survey XPS spectrum of the WB2 sample, High-resolution XPS spectra of (b) W 4f, (c) Bi 4f and (d) O 1s for WB2 sample. (i) WB2 before use; (ii) WB2 after being used to degrade RhB dye for six times.

Adsorption and desorption experiments using N_2 were carried out at 77 K. Fig. 5a displays the nitrogen sorption isotherms of the Bi_2O_3-Bi_2WO_6 heterostructures, pure Bi_2O_3 and Bi_2WO_6 samples. The shape of the isotherm is a type IV isotherm with a type H3 hysteresis loop at high relative pressures according to the IUPAC classification, which indicates that these samples are mesoporous structures in the pore diameter range of 2−50 nm.[33,34] This result can be further confirmed by the corresponding pore size distribution, as shown in Fig. 5b. Considering the observed morphology of the samples, the smaller pores with a sharp peak at about 2.6 nm may be generated during the crystal growth process, whereas the larger pores (20−30 nm) could be generated during thermal treatment process. Table 1 gives the BET surface area and porous volume of different samples. It can be found that the BET specific surface areas of the Bi_2O_3-Bi_2WO_6 p-n junction structures are all higher than that of pure Bi_2O_3 nanorods (1.9 m^2•g^{-1}), but lower than that of Bi_2WO_6 flowers (15.4 m^2•g^{-1}). WB2 and Bi_2WO_6 have much larger pore volume than that of other samples, and Bi_2O_3 nanorods have the smallest pore volume. Previous studies show that a suitable conformation of pores allows light waves to penetrate deep inside the photocatalysts and leads to high mobility of charge.[35-38] It is speculated that the pores in the WB2 heterostructures and Bi_2WO_6 flowers allow the penetration of light waves and phenol or RhB molecules in solution deep into the photocatalysts, which may greatly promote the photocatalytic activity.

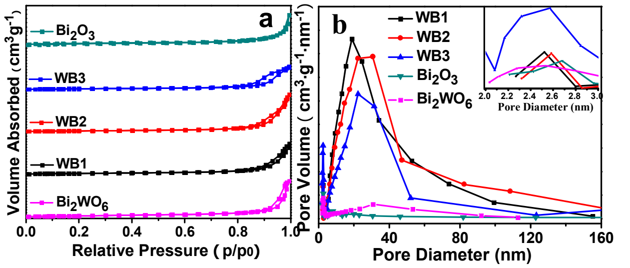

Fig. 5 (a) Nitrogen adsorption-desorption isotherm and (b) the corresponding pore size distribution of the different samples.

Table 1 The surface area surface and pore volume of different samples.

Samples	BET surface area (m^2•g^{-1})	Pore volume (cm^3•g^{-1})
WB1	14.247	0.076
WB2	13.696	0.105
WB3	10.828	0.061
Bi_2O_3	1.891	0.005
Bi_2WO_6	15.426	0.102

The optical property of Bi_2O_3-Bi_2WO_6 heterojunctions was examined using UV-vis diffuse-reflectance spectrum (DRS). As shown in Fig. 6, The absorption edge of the pure Bi_2O_3 and Bi_2WO_6 is ~437 and 428 nm, which shows their visible light absorption. After combining the two semiconductors, Bi_2O_3-Bi_2WO_6 heterojunctions show more intensive absorption within the visible light range in comparison with pure Bi_2O_3 or Bi_2WO_6, and the visible light absorption ability of the composite is gradually enhanced with loaded-Bi_2WO_6 increase. However, too much loaded-Bi_2WO_6 (such as sample WB3) will decrease the visible light absorption. For semiconductors, their optical band gap can be calculated from the absorption spectra using the equation $\alpha h\nu = A(h\nu - E_g)^{2/n}$, in which α, h, ν, A, and E_g are the absorption coefficient, Planck constant, light frequency, a constant and band gap, respectively.[39] In the equation, n decides the characteristics of the transition in a semiconductor, here n = 2 for Bi_2WO_6[40] and n = 4 for Bi_2O_3[41]. The energy of the band gap is calculated by extrapolating the straight line to the abscissa axis. The band gap of pure Bi_2WO_6 and Bi_2O_3 was estimated to be 2.89 and 2.71 eV, respectively.

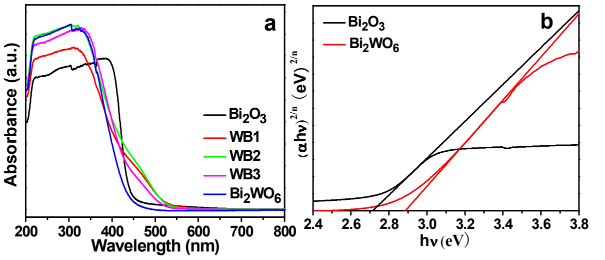

Fig. 6 (a) UV-Vis diffuse reflectance spectra of Bi_2O_3, Bi_2WO_6 and Bi_2O_3-Bi_2WO_6 samples; (b) the plots of $(\alpha h\nu)^{2/n}$ vs. hν (n = 4 for Bi_2O_3 and n = 2 for Bi_2WO_6).

The photocatalytic activity of the samples was evaluated by decomposing toxic organic compounds in aqueous solution, such as phenol. Fig. 7a depicts the correlation curves between the concentration changes of phenol molecules and the irradiation durations in the presence of photocatalysts. It is observed that comparing with pure Bi_2O_3 and Bi_2WO_6, the photocatalytic activities of Bi_2O_3-Bi_2WO_6 p-n junction photocatalysts gradually increase with the loaded-Bi_2WO_6 content increasing and reach the maximum value for WB2 sample. After that, the activity of Bi_2O_3-Bi_2WO_6 p-n junction photocatalyst (WB3) sequentially decreases. Obviously, the photocatalytic activity of the samples is significantly affected by the Bi_2WO_6 content in Bi_2O_3-Bi_2WO_6 junctions. According to the SEM images (Fig. 2) of Bi_2O_3-Bi_2WO_6 p-n heterojunctions, for low Bi_2WO_6 content in WB1 sample, sparse Bi_2WO_6 nanosheets grown on Bi_2O_3 rods are observed, so only a small number of p-n junctions are generated, leading to a low photocatalytic activity. When the Bi_2WO_6 content is increased in the WB2 sample, a large number of p-n junctions are formed, thus resulting in the highest photocatalytic activity for the optimal WB2 sample. With the Bi_2WO_6 content further increasing dense Bi_2WO_6 nanosheets almost cover the Bi_2O_3 rods, as observed in WB3 sample (Fig. 2h), which decreases the light irradiation on Bi_2O_3 rods and the p-n junction interfaces. This shielding effect of dense Bi_2WO_6 nanosheets coating on the Bi_2O_3 rods makes the photocatalytic activity of WB3 sample decrease. When WB2, Bi_2O_3, Bi_2WO_6 and P25 are used as photocatalysts, the degradation efficiencies of phenol are 100%, 44%, 13% and 2% in 60 min under solar light irradiation, respectively. Moreover, when WB2 was used as photocatalyst, the absorption peaks at 270 nm and 208 nm disappeared completely in 120 min (Fig. 7b). The total organic carbon (TOC) was measured, and results show that the phenol molecules can be thoroughly mineralized. Above facts clearly show that the as-obtained WB2 p-n junction structure owns outstanding photocatalytic capacity and can be used in environmental treatment and protection. The UV-vis absorbance spectra of phenol using different samples as photocatalysts are shown in Fig. S3.

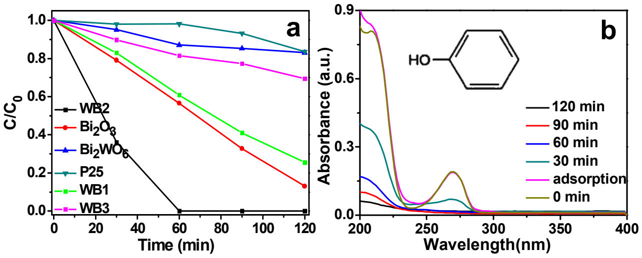

Fig. 7 (a) Photocatalytic degradation curves of phenol (10 mg/L) using different photocatalysts, (b) UV-Vis absorption spectra of phenol using WB2 as phtocatalyst under solar light irradiation.

In order to further evaluate the photodegradation capacity of Bi_2O_3-Bi_2WO_6 p-n junction structures, the degradation of RhB aqueous solution under solar light irradiation was carried out. As shown in Fig. 8a, Bi_2O_3-Bi_2WO_6 p-n junction photocatalysts display better degradation efficiency for RhB than pure Bi_2O_3 and Bi_2WO_6, and WB2 sample displays the best photocatalytical activity which can degrade 100% RhB in 60 min. Moreover, the absorption peaks of the RhB at 554 nm and 200 nm disappear completely after 60 min reaction, and no new peaks appear (Fig. 8b) using WB2 as photocatalyst. This lies in two facts: i) the removal of the ethyl groups and cleavage of the whole chromophore structure (cycloreversion) occur simultaneously for RhB molecules during the photocatalytic process; ii) all RhB molecules are completely degraded. The comparison of the degradation of RhB using Bi_2O_3-Bi_2WO_6 p-n heterojunctions (WB1−WB5) as photocatalysts is given in Fig. S4. It can be found that with the Bi_2WO_6 content increase (WB1 < WB4 < WB2), more and more p-n junctions are formed, which results in the highest photocatalytic activity for the optimal WB2 sample. However, with further increasing the Bi_2WO_6 content (WB2 < WB5 < WB3), dense Bi_2WO_6 nanosheets shield the light irradiation on Bi_2O_3 rods and the p-n junction interfaces and then result in the lowest photocatalytic activity for WB3 sample.

WB2 has also good photocatalytic performance for the degradation of RhB aqueous solution under visible light irradiation (λ > 400 nm) (Fig. S5a), and displays higher photocatalytic activity than Bi_2O_3/Bi_2WO_6 heterostructures reported in ref 24 and 25. However, the degradation mechanism of RhB molecules is different from that under solar light irradiation. The UV-Vis absorbance spectra of RhB molecules (Fig. S5b) after photocatalytic reaction indicate that the removal of the ethyl groups is the first stage and then cleavage of the whole chromophore structure (cycloreversion) occurs in RhB molecules by the visible light irradiation.[42-44, 25]

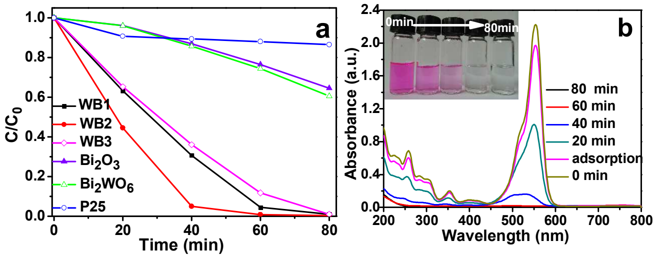

Fig. 8 (a) The degradation curves of RhB using different photocatalysts, (b) UV-Vis absorption spectra of RhB aqueous solutions using WB2 as phtocatalyst under solar light irradiation. Inset in b is photographs of RhB solutions by different reaction time.

To investigate the stability of photocatalytic performance in solar light region, the WB2 sample was used to degrade RhB dye in six repeated cycles, and the results are shown in Fig. 9. It is noteworthy that WB2 photocatalyst exhibits good photostability under solar light irradiation (Fig. 9a), and its photocatalytic efficiency only reduces 2% after six repeated cycles. From the SEM image, we also find that WB2 still retained the original structure (Fig. 9b) after six repeated cycles. The XPS spectrum of the WB2 after being reused for six times to degrade RhB dye is also carried out to prove the photostablility of WB2 sample under solar light irradiation. As shown in Fig. 4 (ii), Bi species are still in the form of Bi^{3+}, and W exists in the form of W^{6+}, demonstrating its high stability in the process of photocatalysis.

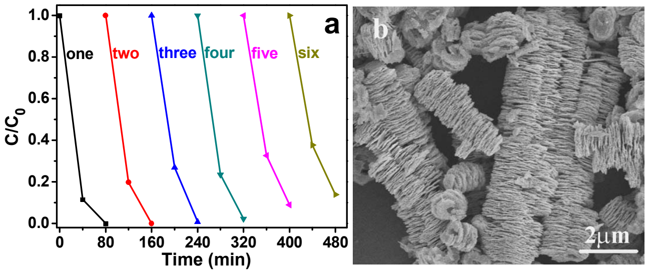

Fig. 9 (a) Cycling times of the photocatalytic degradation of RhB in the presence of WB2 under solar light irradiation, (b) the SME image of the WB2 after six repeated cycles.

To determine the relative positions of conduction band (CB) and VB edges, the total densities of states of VB for Bi_2O_3, Bi_2WO_6 and WB2 were measured, as shown in Fig. 10. In contrast to Bi_2O_3, the VB maximum of WB2 is down-lowered from 1.30 to 1.71 eV. Compared to Bi_2WO_6, the VB maximum of WB2 is up-shifted from 2.24 to 1.71 eV. The shift of VB maximum position for WB2 can be attributed to the formation of heterojunction, as confirmed by XRD and TEM results.

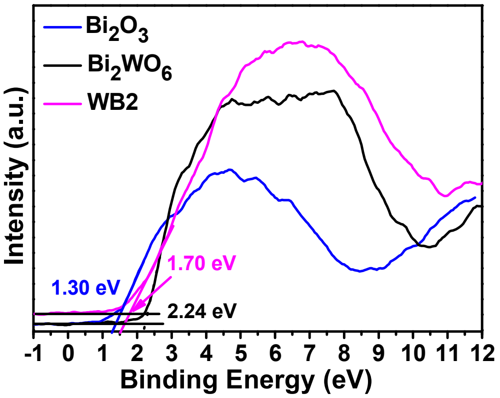

Fig. 10 VB-XPS spectra of Bi_2O_3 and Bi_2WO_6 and WB2 samples.

According to the VB edges of Bi_2WO_6 and Bi_2O_3, and combined with band gap derived from DRS, the CB edge potentials of the two semiconductors can thus be obtained by using the equation of $E_{CB} = E_{VB} - E_g$. So, the energy band structures of Bi_2O_3 and Bi_2WO_6 is easy to be generated (Fig. 11a). For p-type Bi_2O_3, its Fermi energy level is close to the valence band, while for n-type Bi_2WO_6, its Fermi energy level is close to the conduction band. When the two semiconductors are in contact to form p-n junction (Fig. 11b), there is diffusion of electrons from Bi_2WO_6 to Bi_2O_3 due to their different Fermi energy level, resulting in accumulation of negative charges in Bi_2O_3 close to the junction. At the same time, the holes transfer from Bi_2O_3 to Bi_2WO_6, leaving a positive section in Bi_2WO_6 near the junction. Meanwhile, the energy bands of Bi_2O_3 shift upward along the Fermi level and those of the Bi_2WO_6 shift downward along its Fermi level (Fig. 11b). With equilibration of Bi_2O_3 and Bi_2WO_6 Fermi levels, the diffusion of electrons from Bi_2WO_6 to Bi_2O_3 stops. Therefore, an equilibrium state is formed and an inner electric field will also be generated at the interface. Under the solar/visible light irradiation, Bi_2O_3 with narrow band gap is excited and photoelectrons and holes are generated. The excited electrons on the conduction band of p-type Bi_2O_3 transfer to that of n-type Bi_2WO_6, while the holes remain in the valence band of p-type Bi_2O_3. Furthermore, the migration rate of the photogenerated electrons and holes could be promoted by the internal electric field in the Bi_2O_3-Bi_2WO_6 p-n heterojunctions and the photocatalytic activity is largely enhanced.

According to Fig. 10 and Fig. 11, it can be seen that the electronic structure of Bi_2O_3-Bi_2WO_6 p-n junction structure matches well with the redox potential of water into hydrogen and oxygen molecules, namely, the bottom level of the conduct band has to be more negative than the reduction potential of H^+/H_2 (0 eV vs normal hydrogen electrode (NHE)); the top level of the valence band has to be more positive than the oxidation potential of O_2/H_2O (1.23 eV). The experiments of photocatalytic water splitting into O_2 were performed (Fig. S6) using Bi_2O_3-Bi_2WO_6 as photocatalyst. It can be found O_2 production is about 70 mL•g^{-1} in 4 h under 300 W Xe light irradiation.

As well known, many factors influence the photocatalytic activity of a photocatayst, such as BET surface area, size of particles, etc. Prepared Bi_2WO_6 flower owns larger BET surface area than that of WB2, but its photocatlytic activity is much poorer than that of WB2 (Fig. 7, 8). This is mainly attributed to the formation of p-n junction in the WB2 sample.

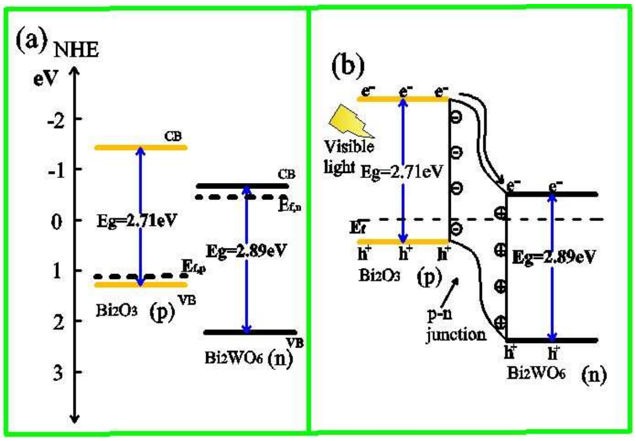

Fig. 11 Schematic diagram for (a) energy band of Bi_2WO_6 and Bi_2O_3 and (b) the formation of p-n junction and the possible charge separation.

Conclusions

In summary, the novel p-n junction photocatalysts of Bi_2O_3 rods-Bi_2WO_6 nanosheets have been prepared for the first time. Bi_2WO_6 nanosheets vertically grow on the Bi_2O_3 nanorods along the axial direction. The obtained Bi_2O_3-Bi_2WO_6 p-n heterojunctions exhibit higher photocatalytic activity than pure Bi_2WO_6 and Bi_2O_3 for the degradation of phenol and RhB under solar/visible light irradiation. Phenol and RhB can be completely degraded in 60 min under solar light irradiation using Bi_2O_3-Bi_2WO_6 p-n heterojunction as photocatalyst. This good photocatalytic activity is ascribed to the synergistic effects: (a) extended absorption in the visible light region; (b) formation of p-n junction enhancing the separation of photogenerated carriers; (c) 1D ordered nanostructure is favourable for high efficient and directional transport and separation of electrons and holes. This study provides a general and effective method to fabricate unique 1D Bi_2O_3-Bi_2WO_6 p-n junction photocatalyst on a large scale. Moreover, this route would offer new insight into the design and fabrication of other advanced materials with heterojunction structures for photocatalytic applications.

Acknowledgements

This work is supported by the special funding support from the the National Basic Research Program of China (2011CB933700, 2010CB934700,) and the National Natural Science Foundation of China (21271165, 21101006).

Notes and references

‡ Additional figures and table are given in supporting information.

1 H. Tong, S. Ouyang, Y. Bi, N. Umezawa, M. Oshikiri and J. Ye, *Adv. Mater.*, 2012, **24**, 229–251.
2 R. Asahi, T. Morikawa, T. Ohwaki, K. Aoki and Y. Taga, *Science*, 2001, **293**, 269–272.

3 Y. Peng, S. C. Qin, W. S. Wang and A. W. Xu, *Cryst, Eng, Comm.,* 2013, **15**, 6518–6525.
4 D. E. Skinner, D. P. Colombo, J. J. Cavaleri and R. M. Bowman, *J. Phys. Chem.*, 1995, **99**, 7853−7856.
5 C. Ye, Y. Bando, G. Shen and D. Golberg, *J. Phys. Chem. B*, 2006, **110**, 15146−15151.
6 D. Chu, J. Mo, Q. Peng, Y. Zhang, Y. Wei, Z. Zhuang and Y. Li, *ChemCatChem*, 2011, **3**, 371−377.
7 X. Zhang, K. Udawa, Z. Liu, S. Nishimoto, C. Xu, Y. Lu, H. Sakai, M. Ave, T. Marakoi and A. Kujishima, *J. Photoch. Photobio. A*, 2009, **202**, 39−47.
8 X. Wang, Q. Xu, M. R. Li, S. Shen, X. L. Wang, Y. C. Wang, Z. C. Feng, J. Y. Shi, H. X. Han and C. Li, *Angew. Chem. Int. Ed.,* 2012, **51**, 13089−13092.
9 T. Kawahara, Y. Konishi, H. Tada, N. Tohge, J. Nishii and S. Ito, *Angew. Chem. Int. Ed.,* 2002, **41**, 2811−2813.
10 X. Wang, S. Shen, S. Q. Jin, J. X. Yang, M. R. Li, X. L. Wang, H. X. Han and C. Li, *Phys. Chem. Chem. Phys.,* 2013, **15**, 19380−19386.
11 H. G. Kim, P. H. Borse, W. Choi and J. S. Lee, *Angew. Chem. Int. Ed.,* 2005, **44**, 4585−4589.
12 B. Nikoobakht, J. Bonevich and A. Herzing, *J. Phys. Chem. C*, 2011, **115**, 9961-9969.
13 C. Zhang and Y. F. Zhu, *Chem. Mater.*, 2005, **17**, 3537−3545.
14 F. Amano, A. Yamakata, K. Nogami, M. Osawa and B. Ohtani, *J. Am. Chem. Soc.*, 2008, **130**, 17650−17651.
15 G. S. Li, D. Q. Zhang, J. C. Yu and M. K. H. Leung, *Environ. Sci. Technol.*, 2010, **44**, 4276−4281.
16 L. Wu, J. H. Bi, Z. H. Li, X. X. Wang and X. Z. Fu, *Catal. Today*, 2008, **131**, 15−20.
17 Z. J. Zhang, W. Z. Wang, M. Shang and W. Z. Yin, *J. Hazard Mater.*, 2010, **177**, 1013−1018.
18 M. K. Lee and T. H. Shih, *J. Electrochem. Soc.*, 2007, **154**, 49−51.
19 Z. L. Xu, I. Tabata, K. Hirogaki, K Hisada, T. Wang, S. Wang and T. Hori, *RSC Adv.,* 2012, **2**, 103−106.
20 Y. Xu and M. A. A. Schoonen, *Am. Mineral*., 2000, **85**, 543−556.
21 L. Zhou, W. Z. Wang, H. L. Xu, S. M. Sun and M. Shang, *Chem. Eur. J.*, 2009, **15**, 1776−1782.
22 M. Ge, Y. F. Li, L. Liu, Z. Zhou and W. Chen, *J. Phys. Chem. C*, 2011, **115**, 5220-5225.
23 X. N. Li, R. K. Huang, Y. H. Hu, Y. J. Chen, W. J. Liu, R. S. Yuan and Z. H. Li, *Inorg. Chem.*, 2012, **51**, 6245−6250.
24 M. S. Gui and W. D. Zhang, *J. Phys. Chem. Solids*, 2012, **73**, 1342−1349.
25 M. S. Gui, W. D. Zhang, Q. X. Su and C. H. Chen, *J. Solid State Chem.*, 2011, **184**, 1977−1982.
26 Z. Q. Li, X. T. Chen and Z. L. Xue, *J. Colloid Interface Sci.*, 2013, **394**, 69−77.
27 Z. Dong, S. J. Kennedy and Y. Wu, *J. Power Sources*, 2011, **196**, 4886−4904.
28 O. Monnereau, L. Torter, P. Llewellyn, F. Rouquerol and G. Vacquier, *Solid State Ionics.*, 2003, **157**, 163-169.
29 W. S. Wang, M. Dahl and Y. D. Yin, Chem. Mater. 2013, 25, 1179−1189.
30 J. Wu, F. Duan, Y. Zheng and Y. Xie, *J. Phys. Chem. C*, 2007, **111**, 12866−12871.
31 Y. Schuhl, H. Baussart, R. Delobel, M. LeBras, J. Leroy, L. G. Gengembre and J. Rimblot, *J. Chem. Soc., Faraday Trans.*, 1983, **79**, 2055-2069.
32 Y. Wang, Y. Wang, Y. Meng, H. Ding, Y. Shan, X. Zhao and X. Tang, *J. Phys. Chem. C*, 2008, **112**, 6620−6626.

33 H. G. Yu, R. Liu, X. F. Wang, P. Wang and J. G. Yu, *Appl. Catal. B*, 2012, **111**−**112**, 326−333.
34 G. I. N. Waterhouse, G. A. Bowmaker and J. B. Metson, *Phys. Chem. Chem. Phys.*, 2001, **3**, 3838-3845.

35 X. Wang, J. C. Yu, C. Ho, Y. Hou and X. Fu, *Langmuir*, 2005, **21**, 2552−2559.
36 L. Z. Zhang and J. C. Yu, *Chem. Commun.*, 2003, **16**, 2078−2079.
37 C. S. Guo, M. Ge, L. Liu, G. D. Gao, Y. C. Feng and Y. Q. Wang, *Environ. Sci. Technol.*, 2010, **44**, 419−425.
38 Y. W. Mi, S. Y. Zeng, L. Li, Q. F. Zhang, S. N. Wang, C. H. Liu and D. Z. Sun, *Mater. Res. Bull.*, 2012, **47**, 2623−2630.
39 M. A. Butler, *J. Appl. Phys.,* 1977, **48**, 1914−1920.
40 Y. Y Guo, G. K. Zhang, H. H. Gan and Y. L. Zhang, *Dalton Trans.,* 2012, **41***,* 12697−12703.
41 H. Y. Jiang, J. J. Liu, K. Cheng, W. B. Sun and J. Lin, *J. Phys. Chem. C*, 2013, **117**, 20029−20036.
42 T. Watanabe, T. Takizawa and K. Honda, *J. Phys. Chem.*, 1977, **81**, 1845−1851.
43 J. D. Zhuang, W. X. Dai and P. Liu, *Langmuir*, 2010, **26**, 9686-9694.
44 K. Yu, S. G. Yang, H. He, C. Sun, C. G. Gu and Y. M. Ju, *J. Phys. Chem. A*, 2009, **113**, 10024−10032.

Graphic Abstract:

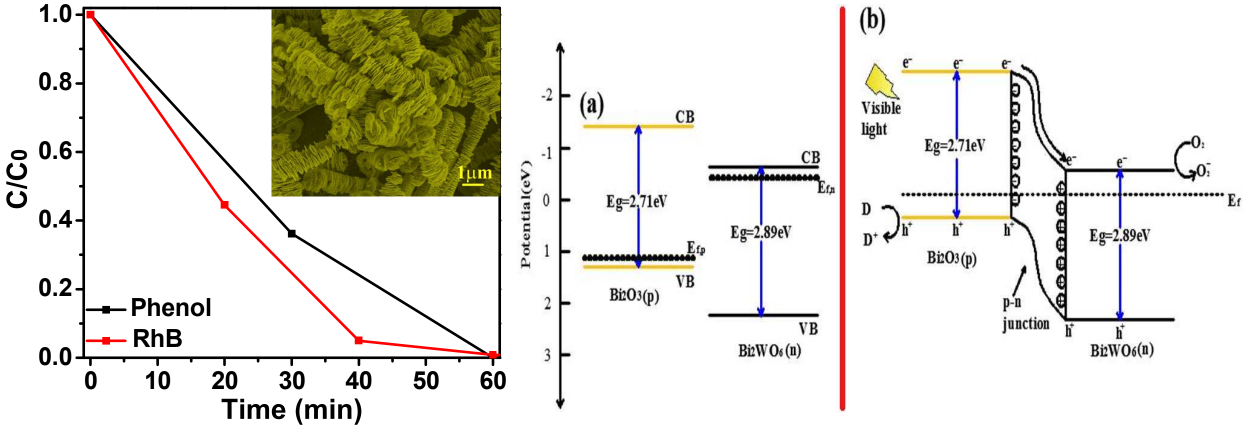

A novel one-dimensional Bi_2O_3 nanorods-Bi_2WO_6 nanosheets p-n junction photocatalyst was prepared. This Bi_2O_3-Bi_2WO_6 heterostructure exhibits high photocatalytic activity for the degradation of phenol and Rhodamine B (RhB) under solar/light light irradiation, which is ascribed to the extended absorption in the visible light region and the effective separation of photogenerated electrons and holes by the internal electrostatic field in the junction region.